ORIGINAL ARTICLE

Madhu Kiran Karanam · Viswanath R. Chinthapenta

Void growth and morphology evolution during ductile failure in an FCC single crystal

Abstract Void growth and morphology evolution are studied using a 3D representative volume element with a spherical void embedded in an FCC single crystal. The plastic flow contours are studied to determine the scenarios leading to fully plastic flow and plastic flow with elastic region. Further, the effect of anisotropy on void growth is studied through three initial crystallographic orientations (ICOs) [100], [110], & [111] with respect to loading direction. Void growth and macroscopic stress variations with applied strain are obtained from our simulations. It is observed that the peak stress corresponds to rapid void growth initiation. The peak stress is found to be dependent on void volume fraction and ICO. Furthermore, an additional geometrical parameter, diagonal distortions (D_{d_i}) is introduced to classify the non-spheroidal void shapes observed in deformed anisotropic crystal.

Keywords Void growth · Void morphology · Ductile failure · Crystal plasticity

1 Introduction

Micromechanical analysis of the ductile failure process is on an increasing trend due to its ability to model the behavior of modern material with complex microstructures effectively. The ductile failure process typically starts with nucleation of voids by fracture and de-cohesion of the second phase particles. The nucleated voids then grow and coalesce to form micro-cracks, which eventually lead to failure of the material. The ductile failure process depends primarily on the geometry of the void (i.e., void shape, void size, distribution of voids), material anisotropy, work hardening, and the stress state around it. Several studies have already been performed to understand this process, both theoretically and experimentally [1–6]. Through the experimental and theoretical studies, the process of void growth is relatively well understood using phenomenological methods. However, the evolution of the morphology of the voids, which is an essential factor in determining the initiation of coalescence and, in turn, the ductile failure, is sparingly studied. A brief of the work in this field is presented here.

The initial theoretical model for void growth was proposed by Rice and Tracey [7], who studied the void growth in the infinite rigid-plastic medium. They observed that under tensile loading with mean stress superposed over it, the volume-changing part of void growth dominates the shape-changing part at higher values of remote stress. However, at lower and moderate values of remote stress, these contributions are equally important. Following that Gurson [1] developed yield function using unit cell model with an isolated cylindrical and spherical void in a rigid-plastic cell for two types of flow field, one with fully plastic flow

M. K. Karanam · V. R. Chinthapenta (✉)
Micromechanics lab, IIT Hyderabad, Kandi, Sangareddy, Telangana 502285, India
E-mail: viswanath@mae.iith.ac.in

(henceforth referred to as Gurson's model-1) and other with plastic flow with rigid region (henceforth referred to as Gurson's model-2). In Gurson's model-2, the extent of rigid region was assumed based on 2D finite element studies [8–10] that were performed using isotropic material. These studies suggested that a part of matrix does not attain plastic yield. Gurson observed that the model-2 had no functional form for the yield locus. Hence, much of the developments of Gurson's work were focused on model-1 [11–15]. Except for few studies on yield criterion near void coalescence from Benzerga and Leblond [16], Keralavarma and Chockalingam [17], and Torki et al. [18]. In these studies, plastic flow was considered limited to the ligament region. Benzerga and Leblond [16] proposed an analytical yield function for porous ductile solid using a cylindrical unit cell containing a coaxial cylindrical void with plastic flow. Keralavarma and Chockalingam [17] extended this work for orthotropic Hill-type matrix using similar unit cell definition. Torki et al. [18] developed an upper bound model and proposed a heuristic modification to capture the behavior of extremely flat or elongated voids. The unit cell definition in these studies was adopted from Thomason [19]. Gurson's work was for isotropic material; however, metals are known to exhibit anisotropic behavior. Therefore, in this study, we are investigating the extent of rigid region in the anisotropic material using crystal plasticity.

Gurson's model and its initial modifications by Tvergaard [20], and later by Mochiet et al. [15] assume that voids are initially spherical, and that shape is preserved during the deformation. However, in reality, initial void shapes are not spherical, and with deformation, the shape tends to change significantly [21–23]. Gologanu et al. [12,13] improved Gurson's model-1 for ellipsoidal voids for prolate and oblate voids. Recently, Madou and Leblond [24] extended Gurson's model-1 for the general ellipsoidal void in an isotropic rigid-plastic matrix.

In line with these theoretical studies, experimental studies were also performed. Crepin et al. [23] performed experiments to demonstrate slip as the underlying mechanisms behind the hexagonal cross section of voids. Babout et al. [25] performed in situ tensile tests and analyzed both local and global void growth using X-ray tomography. While local void growth rates showed a reasonable correlation with analytical models from Rice and Tracey [7], the global void growth rates from Rice and Tracey model were shown to be over predicting. In their experimental study of ductile fracture in steel, Benzerga et al. [26] and Khan and Liang [27] found that all the stages of the process of ductile failure were anisotropic. These are essential inputs for developing an accurate damage mechanics model for predicting ductile failure. In experimental work on the ductile fracture by Morgeneyer et al. [28], on the Al–Cu–Mg sheet, the evolution of void morphology is observed under longitudinal and transverse loading. They found that in the case of longitudinal loading, the voids are strongly prolate and merge in the loading direction, whereas with transverse loading voids close into a penny shaped void. This observation again points towards the strong influence of material anisotropy on the evolution of void morphology. It is important to note that void morphology changes occurring during the progressive deformation tend to determine the mechanism of void coalescence at a later stage in the ductile failure process [29]. Gan et al. [30] analyzed the effect of crystal lattice rotation in an aluminum single crystal under compression loading for a spherical void. Weck et al. [31] conducted the experimental studies by using model microstructures fabricated exclusively for the experiments; they studied the shape evolution of voids using X-ray tomography. And Xu et al. [21] reconstructed the 3D morphology of the void using EBSD with the help of the ion beam and examined the relation with the crystallographic orientation. Lecarme et al. [32] observed large heterogeneity in the void growth rates of individual voids and also found that the local crystal orientation had a significant impact. And more recently, the void growth in titanium was studied by Pushkareva et al. [33] with emphasis on the evolution of its shape and effect of strain localization on it. These experimental investigations provide valuable inputs and validation data for theoretical models (phenomenological and micromechanics-based unit cell models). However, the experimental studies though useful, have the challenges of varying the control parameters effectively to study their influence on the evolution of void morphology and growth rate.

Koplik and Needleman [34] compared the results from Gurson's [1] model-1 with results from their study accounting for void interaction effects and void shape changes and found to be in good agreement. Xia and Shih [35,36], Xia et al. [37], Ruggieri et al. [38], Kuna and Sun [39], Faleskog and Shih. [40], and Faleskog et al. [41] applied unit cell models to calibrate Gurson's [1] model-1 and its modification by Tvergaard [20]. Further developments in the unit cell calculations were considering the influence of the microstructural aspects such as initial crystallographic orientation, crystallographic slip, and strain hardening on void growth and coalescence models performed on single crystal (Gan and Kysar [30], Schacht et al. [42], Potirniche et al. [43], Yerra et al. [6], Yang et al. [44], Ha and Kim et al. [45]).

Potirniche et al. [43] in their study found a strong relationship between void growth rate and void shape distortion with crystal lattice orientation w.r.t the loading direction for single crystals under uniaxial loading. However, under biaxial loading, this effect was observed to be negligible. Ha and Kim [45] and Schacht et al. [42] independently studied the evolution of voids for a single and pair of microvoids at different orientations

in 3D unit cell for FCC single crystal. Ha and Kim [45] studied the effect of initial crystallographic orientation and stress triaxiality on void growth and coalescence. Schacht et al. [42] found that initial crystal orientation affects the formation of deformation bands across the micro-voids. Recently, Ling et al. [46] presented a void growth study for FCC single crystal, which attempted to formulate an elasto-viscoplastic model for porous single-crystals based on unit cell simulations. These studies on single crystals are important as they are ideal for exploring the deformation mechanisms at the grain level. Additionally, in polycrystalline material sometimes voids originate from very small particles (e.g., in high strength steels [47,48]) or voids are embedded in coarse grain (e.g., in coarse-grained Al alloys [49]). In such cases, where the void size is very small compared to the grain size, the plastic activity around the void develops as if it was embedded in a large single crystal. All the above studies focused on the void growth and coalescence were aimed at understanding the impact of either initial crystallographic orientations or the stress triaxiality.

However, no comprehensive study so far has been performed to authors notice on understanding the evolution of void morphology, which plays an important role in the void growth and coalescence as observed in the studies from Weck et al. [31], Xu et al. [21], and Morgeneyer et al. [28]. Hence, in this paper, a generic classification of the void shapes is proposed using additional shape parameter "diagonal distortion" to study the evolving voids with the deformation. And the factors leading to these void shapes are investigated. The study is based on the initially spheroidal void, which grows into different shapes as it deforms. The significant factors affecting the void shape evolution considered are material anisotropy, triaxial boundary strain, and initial size of the voids representing the void volume fraction. Additionally, the void growth evaluated from this study is compared with void growth rate obtained from Rice and Tracey model [7,19].

The regions around the void are investigated, which are either elastic or rigid with respect to the rest of the matrix. A plastic strain (ϵ_p) value of less than 0.2% is considered elastic. The plastic and rigid regions around void are compared with the phenomenological unit cell model from Gurson. This provides fundamental insights to develop phenomenological models for an anisotropic media. The rest of this paper is organized in the following order. Sect. 2 explains the evolution of void morphology. Sect. 3 discusses the methodology used in this study, and results and key conclusions are presented in Sects. 4 and 5, respectively.

2 Evolution of void morphology

Void growth is a non-homogeneous deformation process. Voids tend to evolve into different morphologies as they grow under applied stress or strain field. The void growth and onset of void coalescence are functions of the initial shape of the void and its evolution with load, void size, strain hardening, and stress triaxiality [7,12,13,19,50–52]. Rice and Tracey's void growth model included the effect of dilatation and void shape using amplification factors, D and (1 + E), respectively. The contribution from the void shape change part was found to be significant for low and moderate stress triaxialities (see Huang 1991b [53] for void growth at low-stress triaxiality). Gurson-Needleman-Tvergaard model is an extension of Gurson's model-1 by Needleman and Tvergaard in 1984 [11]. They introduced heuristic parameters to predict the void growth rates accurately. Gologanu-Leblond-Devaux [12,13] proposed a rate based void evolution model which was later extended by Pardoen and Hutchinson [50] to include the strain hardening effects and criterion for onset of coalescence. Ragab [51] reviewed and consolidated the studies on the void shape evolution and developed a set of semi-empirical laws using a total strain formulation. These laws were a function of nucleation strain, equivalent plastic strain, initial void aspect ratio, hardening exponent, and stress triaxiality. Gologanu et al. [12] proposed an equation for the aspect of the void termed as a shape parameter. The shape parameter is particularly of interest for coalescence studies. The coalescence of voids depends on the void spacing and the void shape. The shape parameter ξ_i, is defined as

$$\xi_i = \ln\left(\frac{R_2}{R_i}\right) ; i = 1,\ 3 \tag{1}$$

Where, R_i are the void radii in the transverse principal directions (refer to Fig. 1) and R_2 is void radius in principal loading direction. Gologanu et al. [12] proposed a relation for $\dot{\xi}$ using following Eq. (2) given as:

$$\dot{\xi} = h(D_{33} - D_{11}) + 3\left(\frac{1 - 3\alpha_1}{f} + 3\alpha_2 - 1\right)D_m,$$
$$\alpha_1 \equiv \alpha\left(e_1\right), \alpha_2 \equiv \alpha\left(e_2\right) \tag{2}$$

Where D_{11} and D_{33} are the components of macroscopic strain rate, $D_m \equiv \frac{1}{3} tr\mathbf{D}$, e_1 and e_2 are the eccentricities of void and unit cell, and h is an empirical factor which depends on the void eccentricity, e and stress triaxiality, T. And it is defined as:

$$h(e_1, T) = 2 - T^2 + \left(T^2 - 1\right)e_1^2 \tag{3}$$

For a spherical void in confocal matrix, the rate of the shape parameter, $\dot{\xi} = 0$ as $\alpha_1 = \alpha_2 = \frac{1}{3}$. In their study, the initial void shape and void shape change with deformation is spheroidal. However, non-spheroidal void shapes post deformation are observed in the experimental and numerical studies such as [23,28,31,45, 54,55]. The details of the non-spheroidal void shapes post-deformation and classification of its morphology are discussed in Sect. 4.3 using newly introduced parameter. Additionally, studies were based on the isotropic elasto-plastic material, which fails to account for the microscopic effects such as slip interaction, lattice spin, orientation effects, and strain hardening (except for [50] which included strain hardening). Accurate representation of material anisotropy is inherently accounted for by using crystal plasticity based constitutive model as it considers the slip systems in single crystals. Crystal plasticity framework used in the study is described in Sect. 3.1. The present study focuses on hardening in the regime where plastic strains dominate over elastic strain. The slip on a slip system is initiated when the resolved shear stress (the Schmid stress) on the slip system is more than the critical resolved shear stress. Non-Schmid phenomena such as diffusion and twinning are not considered as these are not common in FCC copper single crystal. Section 3.1 describes the material hardening law.

3 Methodology

3.1 Constitutive relation for single crystal

The finite element based study of the void growth in single-crystal (FCC) requires a constitutive theory based on crystal plasticity that accurately describes the kinematics and kinetics of the crystal behavior in deformation. The theory for kinematics of crystal plasticity used in this paper follows the approach from Hill, Rice, and Asaro [56–58]. The implementation is similar to that of Huang 1991 [59] and Kysar and Hall 1997 [60]. Deformation gradient is defined by $\underline{F} = \partial \underline{x} / \partial \underline{X}$ where, $\underline{X}$ is the initial configuration and $\underline{x}$ the current configuration. The deformation gradient is split into elastic and plastic parts through multiplicative decomposition into the form $\underline{F} = \underline{F}^e \underline{F}^p$. Further, the velocity gradient with respect to the current configuration $\underline{x}$ is given by $\underline{L} = \partial \underline{v} / \partial \underline{x}$ and the elastic and plastic parts of the velocity gradient are written as, $\underline{L} = \underline{L}^e + \underline{L}^p$ where $\underline{L}^e = \dot{\underline{F}}^e \underline{F}^{e-1}$ and $\underline{L}^p = \underline{F}^e \dot{\underline{F}}^p \underline{F}^{p-1} \underline{F}^{e-1}$.

The constitutive behavior of the single crystal determined by the flow rule, hardening law, and the stress–strain response describes the kinetics:

$$\overset{\triangledown}{\underline{\tau}} = \underline{\underline{C}}^e : \underline{D}^e \text{ and } \underline{D}^e = \frac{1}{2}(\underline{L}^e + \underline{L}^{e^T}) \tag{4}$$

Where, $\underline{\tau}$ is the second Piola-Kirchhoff stress, related to the Cauchy stress $\underline{\sigma}$ by $\underline{\tau} = |\underline{F}| \underline{\sigma}$ and $\underline{\underline{C}}^e$ is the IVth order elastic stiffness tensor in the global system of coordinates. The resolved shear stresses on the slip systems α are given by

$$\underline{\tau}^\alpha = \underline{\sigma} : \underline{P}^\alpha \tag{5}$$

Where $\underline{P}^\alpha = sym(\underline{s}^\alpha \underline{m}^\alpha)$ is the Schmid tensor for every slip system α, and $\underline{s}^\alpha$ and $\underline{m}^\alpha$ are the slip direction and slip plane of the slip system, respectively. For FCC crystals, crystallographic slip is assumed to occur on the $\langle 110 \rangle \{111\}$ slip systems. The components of the slip plane normal and slip direction are presented in Table 1. The plastic part of the velocity gradient, for a slip rate $\dot{\gamma}^\alpha$, on the slip systems is

$$\underline{L}^p = \sum_\alpha \dot{\gamma}^\alpha \underline{P}^\alpha \tag{6}$$

The plastic slip rate $\dot{\gamma}^\alpha$ is defined in terms of resolved shear stress as

$$\dot{\gamma}^\alpha = \dot{k}^\alpha \left(\frac{\underline{\tau}^\alpha}{\underline{g}^\alpha}\right) \left|\frac{\underline{\tau}^\alpha}{\underline{g}^\alpha}\right|^{n-1} \tag{7}$$

Table 1 Designation of slip systems in FCC single crystal [63]

Slip plane	(111)			$(1\bar{1}\bar{1})$			$(\bar{1}11)$			$(1\bar{1}1)$		
Slip direction	$[0\bar{1}1]$	$[10\bar{1}]$	$[\bar{1}10]$	$[011]$	$[\bar{1}\bar{1}]$	$[1\bar{1}0]$	$[0\bar{1}1]$	$[\bar{1}\bar{1}]$	$[110]$	$[011]$	$[10\bar{1}]$	$[\bar{1}\bar{1}0]$

Where n is the rate sensitivity exponent. Constant $\dot{k}^{\alpha}$ is the reference strain rate on slip system α, g^{α} is the current strength of the slip system α. The strain hardening is characterized by the evolution of the current strength $\underline{g}^{\alpha}$ of the slip system α through the incremental relation:

$$\underline{g}^{\alpha} = \sum_{\beta} h_{\alpha\beta} \dot{\gamma}^{\beta} \tag{8}$$

Where $h_{\alpha\beta}(\alpha \neq \beta)$ is the latent hardening modulus and β is number of activated slip systems and $h_{\alpha\alpha}$ (no sum) is the self hardening modulus. The latent hardening modulus is given by $h_{\alpha\beta} = qh(\gamma)$ $(\alpha \neq \beta)$ where q is constant. The hardening modulus $h_{\alpha\alpha}$ is proposed by Pierce, Asaro, and Needleman [61],

$$h_{\alpha\alpha} = h(\gamma) = h_0 \text{sech}^2 \left| \frac{h_0 \gamma}{(\tau_s - \tau_0)} \right| (no\ sum\ on\ \alpha) \tag{9}$$

Where, h_0 is hardening modulus at initial yield, τ_0 is the initial yield stress, τ_s is the stage I stress, and γ is Taylor's cumulative shear strain on all the slip systems defined as

$$\gamma = \sum_{\alpha} \int_0^t |\dot{\gamma}^{(\alpha)}| dt \tag{10}$$

This definition of γ generalizes the hardening law in Eq. (8) suitable for single slip to multiple slip situation. Pierce et al. 1982 [61] showed a good fit for this hardening behavior with experiments from Chang and Asaro 1980 [62]. This hardening law is henceforth represented as Power law Crystal Hardening Behavior (PCHB).

Plastic flow on a slip system α commences when $\tau^{\alpha} \geqslant \tau_{cr}^{\alpha}$, where τ_{cr}^{α} is the critical shear stress value. The slip systems on which the conditions are met are the critical slip systems where

$$\dot{\tau}^{(\alpha)} = \dot{\tau}_{cr}^{(\alpha)} = \Sigma_{\beta=1}^{N} h_{\alpha\beta} \dot{\gamma}^{(\beta)} \text{ if } \dot{\gamma}^{(\alpha)} > 0 \tag{11}$$

and,

$$\dot{\tau}^{(\alpha)} < \dot{\tau}_{cr}^{(\alpha)} = \Sigma_{\beta=1}^{N} h_{\alpha\beta} \dot{\gamma}^{(\beta)} \text{ with } \dot{\gamma}^{(\alpha)} = 0 \tag{12}$$

The inequality for non-critical systems is, $\tau^{\alpha} < \tau_{cr}^{\alpha}$ with $\dot{\gamma}^{(\alpha)} = 0$. Where N is the number of slip systems.

3.2 Problem formulation

The mechanics of void growth and shape evolution is studied using a representative volume element (RVE) shown in Fig. 1. The RVE consists of a single spherical void embedded in the matrix material assumed to be FCC single crystal that is modeled using constitutive relation described in Sect. 3.1. Slip systems for FCC single crystal considered in this study are $\langle 110 \rangle$ $\{111\}$ see Table 1 for details. The RVE is subjected to a triaxial strain by applying a displacement along X_1, X_2, and X_3 directions. A displacement value of δ is applied along X_2 direction and corresponding displacement of $\Gamma\delta$ is applied along X_1 and X_3 directions. Where, Γ is the displacement ratio (see Fig. 1), it is defined as ratio of displacement in X_3 (X_1) direction to X_2 direction. Several previous studies on void growth and coalescence used boundary conditions to keep the stress triaxiality constant [6,34,39,45]. However, in this study, the strain-controlled boundary conditions are used which resulted in high stress triaxiality that varied with the applied strain. Further, these boundary conditions provide reliable results in the post-cavitation (rapid void growth) regime. [40]. Similar boundary conditions were used by . [40,42–44,64]. For the present study following values of displacement ratio, $\Gamma = -0.75$ and -0.25 were employed. These values correspond to a cell volume change of $\pm 5\%$, respectively. The selection of displacement ratio in this manner allows for studying the void growth as well as void shrinkage.

Two coordinate systems are used in the study one represents the global or specimen coordinate system and other the local or crystal coordinate system. Prior to loading, the orientation of the crystal axes with respect to
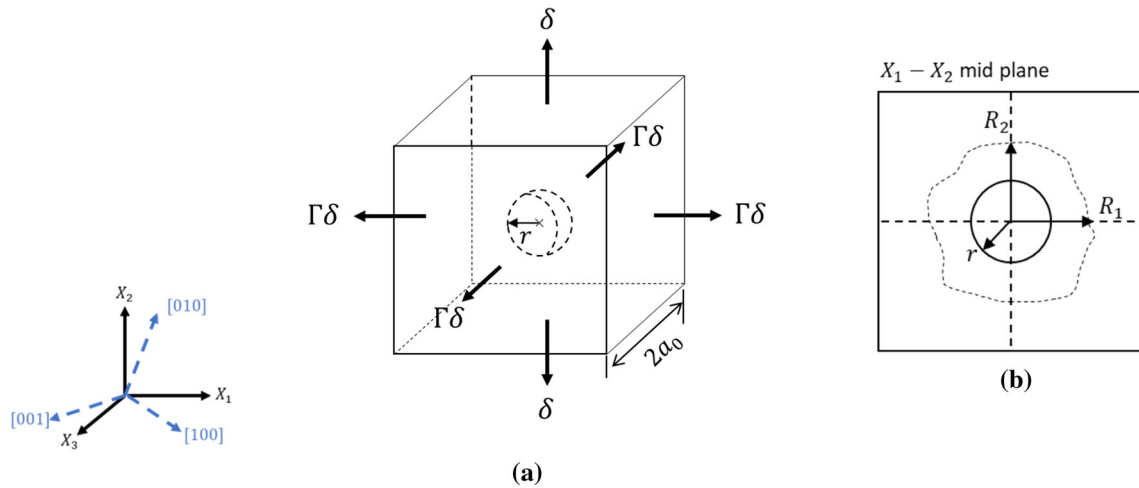
Fig. 1 **a** Schematic of RVE describing the boundary conditions and initial crystallographic orientation. There are two coordinate systems shown in the figure corresponding to the RVE orientation (solid line) and initial crystallographic orientation (dotted line). The orientation of the crystal axes with respect to the global loading direction (X_2), represents the initial crystallographic orientation. **b** Radius of the initial spherical void and radii of deformed void on $X_1 - X_2$ mid plane
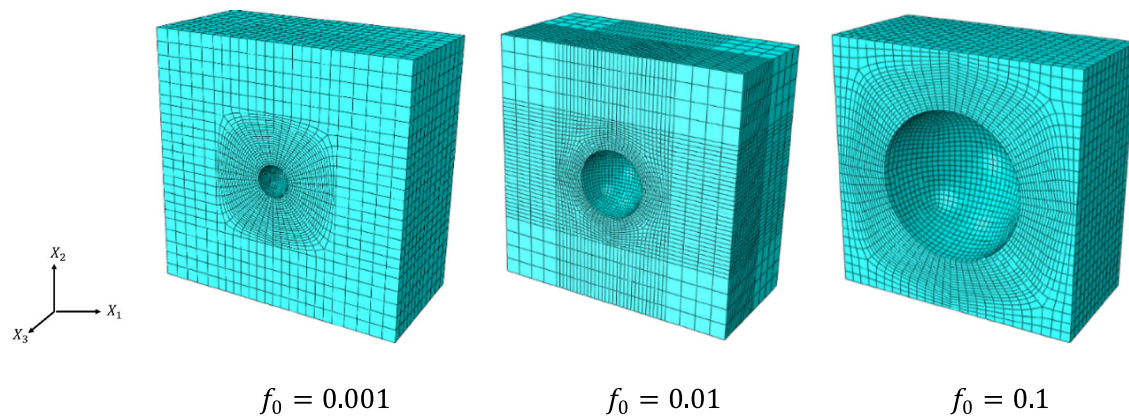

$$f_0 = 0.001 \qquad f_0 = 0.01 \qquad f_0 = 0.1$$

Fig. 2 Cut section of the FE model of the representative volume element for three void volume fractions

the global loading direction (X_2) represents the initial crystallographic orientation (ICO). Nomenclature used for the initial crystallographic orientation [lmn] is similar to the Muller index notation for the crystallographic direction. Three different crystal orientations: [100], [110], and [111] are considered in this study. More specifically, when the initial crystallographic orientation is [100], the crystal axis [100] aligns with the loading axis X_2. As we assumed a spherical void, one of the principal axes of the undeformed void coincides with the loading direction. Three different sizes of the void with respect to the RVE length ($r_0/a_0 = 0.149$, 0.067, 0.031) are used in the study. These void sizes represent the void volume fraction through the relation $f_0 = \frac{4}{3}\pi \left(\frac{r_0}{2a_0}\right)^3$ where f_0 is the initial void volume fraction, r_0 is the radius of the undeformed void, and a_0 is the half-length of the side of the enclosing cube. Therefore, representative void volume fraction values for the void sizes considered are $f_0 = 0.001$, 0.01 and 0.001. The initial void volume fraction values of $f_0 = 0.01$ and 0.001 are apt for studying crystalline metals, whereas the initial void volume fraction of 0.1 is relatively large for crystalline metals; however, such large values of the void volume fraction are possible in porous material [51], for which this study may only apply qualitatively.

Three FE models representing three void sizes are shown in Fig. 2. The mesh is generated out of C3D8 elements in ABAQUS, the constitutive model for the crystal plasticity is applied through a user subroutine UMAT in ABAQUS standard [59,60]. As simulations are computationally expensive, commercial FE software ABAQUS with parallel processing is used instead of serial inhouse FE code. Each FE model is checked for

Table 2 Material parameters for power law crystal hardening behavior (PCHB) [61,65]

C_{11}	C_{12}	C_{44}	n	$\dot{\gamma}$	h_0	τ_0
170 GPa	123 GPa	75.2GPa	10	0.001	541.48 MPa	60.84 MPa
τ_s	q	q_1				
109.51	1	0				
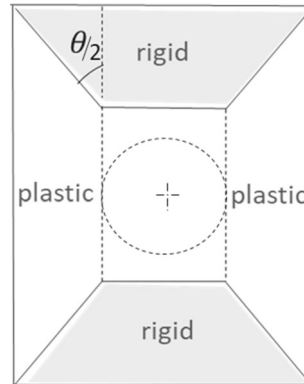
Fig. 3 Rigid (shaded) and plastic regions in the phenomenological model from Gurson [1]

the mesh convergence, which is achieved with 31104 elements for $f_0 = 0.001$, 62552 elements for $f_0 = 0.01$, 50376 elements for $f_0 = 0.1$.

The material parameters for FCC copper single crystal used in this study are listed in Table 2 the values of the parameters are adopted from Pierce et al. 1982 [61] and Jacobsen 1954 [65].

Where q and q_1 are constants representing ratio of latent to self-hardening moduli within same and different set of slip systems, respectively. The values of $q = 1$ (Taylor's hardening) and $q_1 = 0$ (as there is only one set of slip system for FCC) are used in this study. The macroscopic stress components Σ_i $(i = 1, 2, 3)$ are taken as total normal force on the RVE face divided by the current total area of the face. Note that $\Sigma_1 = \Sigma_3 \neq \Sigma_2$. The macroscopic mean stress, $\Sigma_m = \frac{\Sigma_1 + \Sigma_2 + \Sigma_3}{3}$ and macroscopic equivalent stress is taken as $\Sigma_{eq} = |\Sigma_2 - \Sigma_1|$.

This study is performed for factors namely initial void volume fraction values ($f_0 = 0.001$, $f_0 = 0.01$, $f_0 = 0.1$), ICO ([100], [110], [111]), and displacement ratios ($\Gamma = -0.25$, $\Gamma = -0.75$) for PCHB represented by Eq. (9).

4 Results and discussions

4.1 Plastic flow contours during void growth

The phenomenological unit cell models, such as the one proposed by Gurson [1], Benzerga and Leblond [16], and Keralverma and Chockalingam [17] for upper bound yield function were derived assuming rigid-plastic matrix material. The unit cell definition in these models was either based on fully plastic flow (Gurson's model-1) or plastic flow with rigid region (Gurson's model-2), see Section 1. Schematic of the model from Gurson [1] is shown in Fig. 3. The figure is a reconstruction from Gurson's [1] work for an equivalent unit cell. The unit cell is a void matrix aggregate with shaded conical region (top and bottom of void) representing regions that did not attain plastic yield idealized here as rigid. Where, $\theta/2$ is the half-angle of the rigid-plastic transition boundary w.r.t vertical axis. As discussed in Sect. 1, the rigid plastic region in Gurson's model-2 is based on observations from numerical studies, which show that some portion of the unit cell remains elastic during deformation.

Figures 4 and 5 show cumulative shear strain plots on the cross section of the 3D RVE taken on mid-plane $X_1 - X_2$ at 5% applied strain. The gray color contour represents elastic region ($\gamma < 0.002$). The cumulative shear strain over all slip systems (γ) is defined in Eq. (10) and the 5% applied strain corresponds to rapid void growth stage, the details about rapid void growth will be discussed later in Sect. 4.2. The parameters used
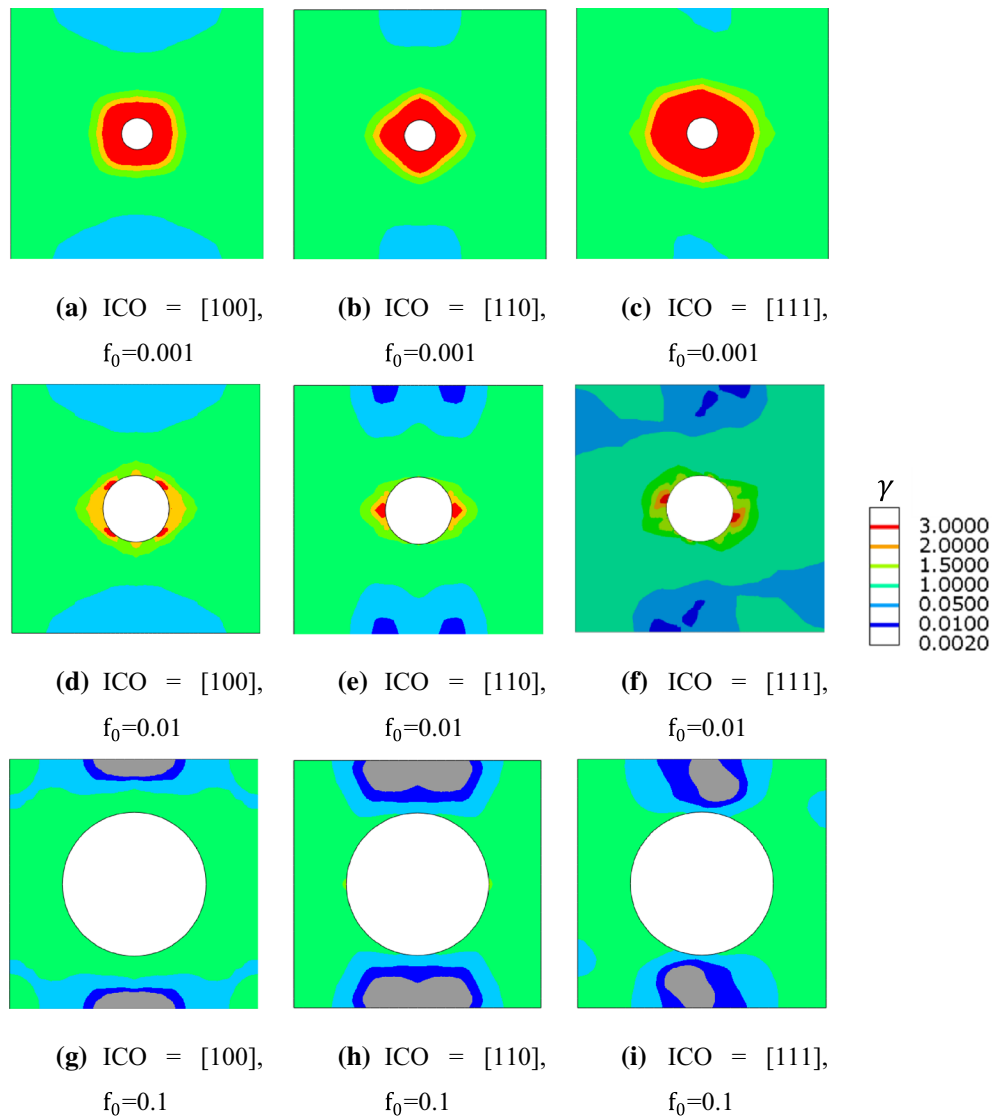
Fig. 4 The cumulative shear strain plots at 5% applied strain for displacement ratio, $\Gamma = -0.25$

in these figures, initial void volume fraction (f_0), displacement ratio (Γ), and ICO are described in detail in Sect. 3.2.

For $\Gamma = -0.25$, intense shear strain localization is observed near the void, with steep gradient towards the boundary of RVE for smaller void volume fraction of $f_0 = 0.001$. Results indicate that the cumulative shear strain field near void changes significantly with ICO, see Fig. 4a–c. Peak plastic strain of 8.0 is observed for applied remote strain of 0.05 and is distributed around the void positioned at $\pm 45°$ from the loading direction for ICO [100] orientation. The maximum shear strain regions are located along the ligament region for ICO [110]. And for ICO [111], the maximum shear strain region is inclined at an angle to the horizontal. These patterns are more evident when the results are seen together with that for the void volume fraction of $f_0 = 0.01$, see Fig. 4d–f.

In the case of $f_0 = 0.01$, the peak cumulative shear strain value of 3.0 for an applied remote strain of 0.05 is observed and the spread is limited to a small region around the void. This kind of shear strain localization is however not seen for the larger void volume fraction of $f_0 = 0.1$, see Fig. 4g–i. For $f_0 = 0.001 \& 0.01$, the material shows a fully plastic flow for all the ICOs and the behavior is similar to the Gurson's model-1. However, for $f_0 = 0.1$ a portion of unit cell remains elastic at applied remote strain of 0.05 with the spread of elastic region approximately inside a truncated cone with included angle, $\theta \approx 60°$. This behavior is closer

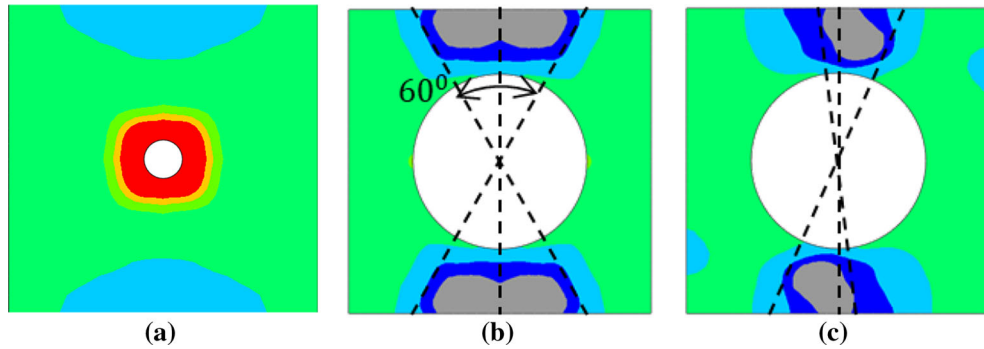**Fig. 5** Spread of elastic region described by angle θ: **a** Fully plastic flow in line with Gurson's model-1. **b** Plastic flow with elastic region, contained within a cone angle of $\theta \approx 60^0$, similar to Gurson's model-2. **c** The elastic region of irregular shape (gray contour), which follows neither Gurson's model-1 nor model-2

to Gurson's model-2. The results for $\Gamma = -0.75$ shows a fully plastic flow for all the parameters considered (the plots are not shown in this paper for brevity).

The extent of the elastic region up to 5% applied strain from this study is summarized in Fig. 5(a–c). In the current study, the type of flow field in matrix material varies from fully plastic flow (Gurson's model-1) to plastic flow with elastic region (Gurson's model-2). For ICO [100] and [110], the shape of the elastic region is conical, but for ICO [111], the shape of the elastic region is irregular, see Fig. 5c. The elastic region positioned at the top and bottom of void is in a conical zone of $\theta \approx 60°$. It shows that Gurson's model-2 is valid for ICO [100] and [110] in developing a phenomenological model in an anisotropic material. Further, the spread of elastic region is observed to be sensitive to the selected ICO and f_0.

4.2 Void growth

In this section, the results from the simulations were analyzed to understand the effect of material anisotropy, initial void volume fraction (f_0), and displacement ratio (Γ) on the void growth. Figures 6, 7, and 8 compare the mean void growth from the CPFEM simulation ($\bar{R}_{sim}$) to analytical mean void growth ($\bar{R}$) obtained using integrated form of the Rice and Tracey mean void growth rate for initially spherical void by Thomason [19]. Where $\bar{R}_{sim} = mean\,(R_\omega)$ where ω is set of all nodes on the void surface and $\bar{R}$ is given by Eq. (13)

$$\bar{R} = \exp\,(D\epsilon_2)\,R_0 \tag{13}$$

Where, R_0 is the initial radius of the spherical void, ϵ_2 is the total applied strain on the RVE in tensile direction and D is defined as

$$D = 0.558\,sinh\left(\frac{3}{2}\frac{\sigma_m}{\sigma_Y}\right) + 0.008\cosh\left(\frac{3}{2}\frac{\sigma_m}{\sigma_Y}\right) \tag{14}$$

Where, $\frac{\sigma_m}{\sigma_Y} = T$ and T is the stress triaxiality. The parameter D is used by Rice and Tracey to account for the volume changing part of the void growth. The evolution of the mean radius of void is related to stress triaxiality through parameter D defined in Eq. (14). To calculate the analytical mean void growth, stress triaxiality from the simulations is required. However, the stress triaxiality vs. applied strain for a given initial void volume fraction (f_0) is different for each ICO. Hence, only two values of stress triaxiality ($T = 0.33\,\&\,3.0$) are considered to evaluate analytical mean void growth from Eq. (13). The lower level of stress triaxiality ($T = 0.33$) corresponds to uniaxial tension [66] and higher level of stress triaxiality ($T = 3.0$) is typical of a blunting crack tip [67].

The mean void growth and the normalized macroscopic stress (Σ_2/σ_Y) variation with applied strain for displacement ratio of $\Gamma = -0.25$, ICO [100], and $f_0 = 0.1,\ 0.01,\ \&\ 0.001$ for PCHB are presented in Fig. 6a and b.

Initial void volume fraction is observed to have a significant effect on the mean void growth, i.e., smaller void leads to higher void growth and vice versa. [40,45], see Fig. 6a. It is also observed that the growth of the initially smaller void exhibits three different regimes of void growth. The first stage is characterized by slow void growth, followed by a stage of rapid void growth and then the third stage, where a reduced void
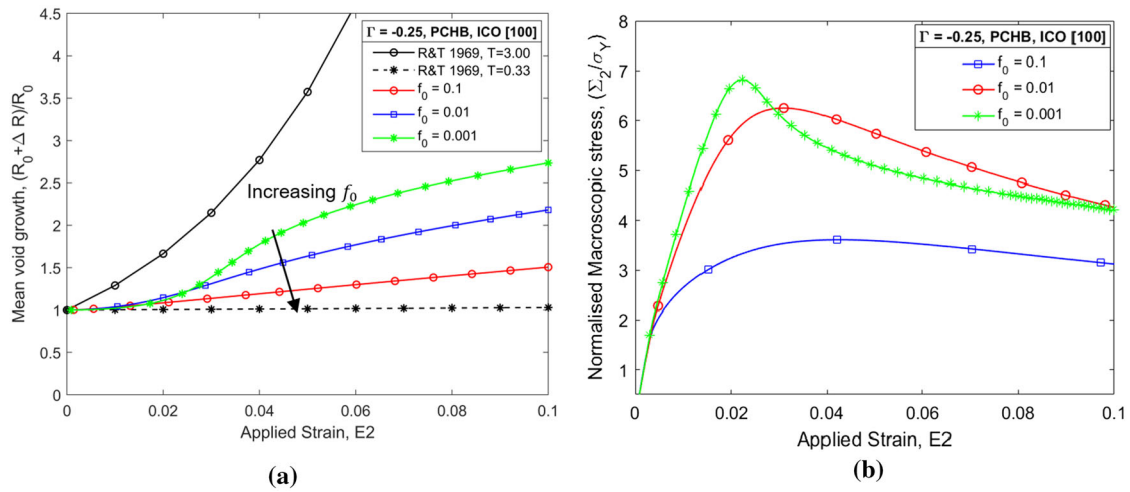
Fig. 6 Comparison of **a** mean void growth vs. applied strain, and **b** normalized macroscopic stress vs. applied strain for three values of initial void volume fractions ($f_0 = 0.1,\ 0.01,\ \&\ 0.001$), $\Gamma = -0.25$ and ICO [100]
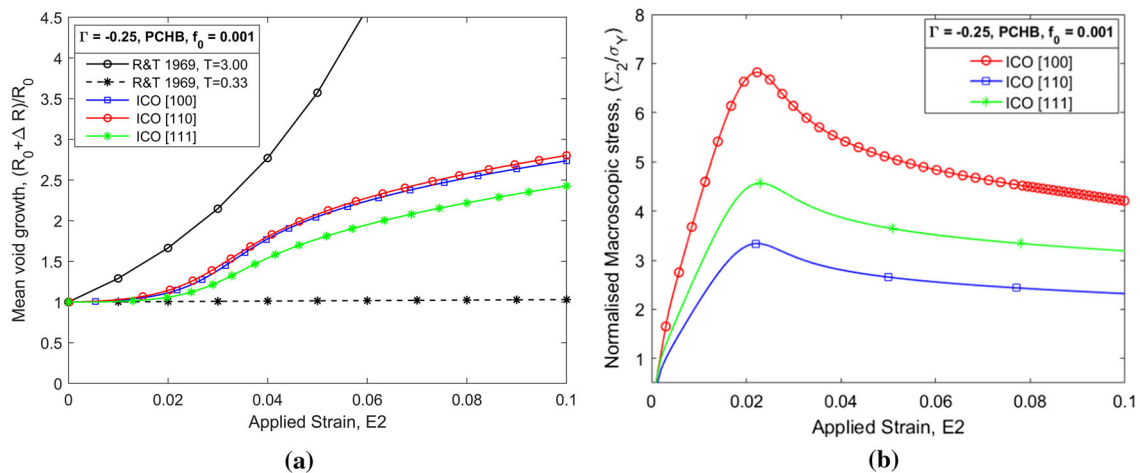

Fig. 7 Comparison of **a** mean void growth versus applied strain, and **b** normalized macroscopic stress versus applied strain for ICOs [100], [110], and [111], $\Gamma = -0.25$ and $f_0 = 0.001$

growth is observed. [40]. Looking at Fig. 6b, it is observed that the initiation of the rapid void growth occurs at peak macroscopic tensile stress around 2% applied strain for $f_0 = 0.001$. This stage continues until void growth starts reducing again and fall in the stress–strain curve starts to become less steep. It is more evident for the smaller void, but as the void size increases, the mean void growth curves tend to become monotonic (see Fig. 6a).

The mean void growth from our study is found to be within the two extrema of the void growth rate obtained from the Rice and Tracey analytical model for low-stress triaxiality ($T = 0.33$) and high-stress triaxiality ($T = 3.0$). Our predictions of the void growth rate are essentially lower than the analytical predictions with high triaxiality ($T = 3.0$). Rice and Tracey void growth model assumes a void embedded in a material with an infinite extent, and the load applied was remote stress or strain fields. This assumption points towards infinitesimally small void. From our results, it is observed that the void growth depends on the void volume fraction inversely and that the Rice and Tracey void growth analytical model would form a limiting case for estimation of void growth with void volume fraction tending towards zero. This shows that Rice and Tracey's model provides a conservative estimate of void growth.

Figure 7a compares the mean void growth for different ICO for void volume fraction of $f_0 = 0.001$, $\Gamma = -0.25$, and PCHB. It is observed that the mean void growth obtained for ICOs [100] & [110] are comparable, with the maximum difference between the two mean void growth values around 2.2%, whereas
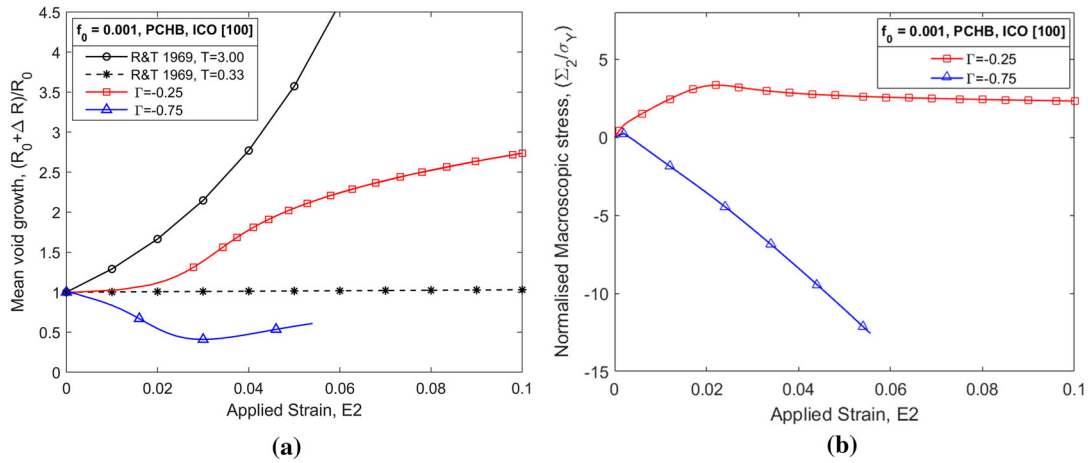
Fig. 8 Comparison of **a** mean void growth vs. applied strain, and **b** normalized macroscopic stress versus applied strain for $\Gamma = -0.25$ and -0.75, $f_0 = 0.001$ and ICO [100]

for the ICO [111], the difference with the other two ICOs is approximately 13.5%. Figure 7b shows the normalized stress vs. applied strain for the same simulations as in Fig. 7a. The normalized stress–strain curve increases with increasing strain and peaks at a critical applied strain. The peak stress represents initiation of the rapid void growth, see Fig. 7a. Beyond the peak stress, the softening due to void growth dominates the hardening provided by the material. The normalized peak stress of 6.81, 4.57 and 3.34 for ICO [100], [110] and [111] is observed, respectively. It shows that the normalized peak stress is dependent on ICO, with maximum peak stress observed for ICO [100] and minimum for ICO [111]. Yang et al. [30] studied the effect of crystallographic orientations on the void growth using a 3D unit cell at $\Gamma = -0.235$. Also observed that for ICO of [100] and [110] the void growth was similar; however for ICO [111] the void growth was shown to be lower than that for the ICO [100] and [110], whereas Potriniche et al. [43] observed less influence of ICO on void growth for bi-axial loading for a single void embedded in FCC single crystal.

Figure 8a compares the mean void growth and shrinkage for $f_0 = 0.001$, PCHB and ICO [110] for two displacement ratios of $\Gamma = -0.25 \, \& -0.75$. The void grows for $\Gamma = -0.25$ while it collapses to a penny shaped crack for $\Gamma = -0.75$. The void shrinkage is observed consistently for $\Gamma = -0.75$ with all three-initial void volume fraction and ICOs. Void shrinkage can also be attributed to cell volume reduction seen for $\Gamma = -0.75$. In Fig. 8b, a comparison of the normalized macroscopic stress (Σ_2/σ_Y) vs. applied strain (E_2) is shown for same set of simulations as discussed in Fig. 8a. The normalized macroscopic stress (Σ_2/σ_Y) for $\Gamma = -0.75$ is significantly negative as this loading represents cell volume shrinkage. In fact, in our study void shrinkage is only observed for $\Gamma = -0.75$. A similar observation was also seen in Budiansky et al. 1982 [68]; they noted that the void growth or shrinkage exclusively depends on the remote stress independent of the initial void size and aspect.

Figure 9a, b shows a comparison of void growth and shrinkage for $f_0 = 0.01 \, \& \, 0.1$ captured at 10% applied strain for $\Gamma = -0.25 \, \& -0.75$, ICO [100], and PCHB. For $\Gamma = -0.75$, both the figures show void shrinkage (black contour), while $\Gamma = -0.25$, represents void growth (red contour).

Figure 10 shows the hydrostatic pressure distribution for the same set of simulations presented in Fig. 9a. In Fig. 10a, the stress field near the void shows negative hydrostatic pressure around the void that leads to void growth. While in Fig. 10b, the stress field near the void shows positive hydrostatic pressure around the void that leads to void growth.

4.3 Classification of void morphology

Void shape evolution is at first studied from the experimental and unit-cell based works from literature, and five most commonly occurring void shapes are identified and recreated using CPFEM simulations. The void shapes obtained are listed in Figs. 11 and 12. In this section, our interest is to study the void shapes and not the stress state near the voids; the stress contours shown in Figs. 11 and 12 do not have any significance. However, stress contours are retained for better visualization. Initial void shapes are spheroidal and non-spheroidal in nature;
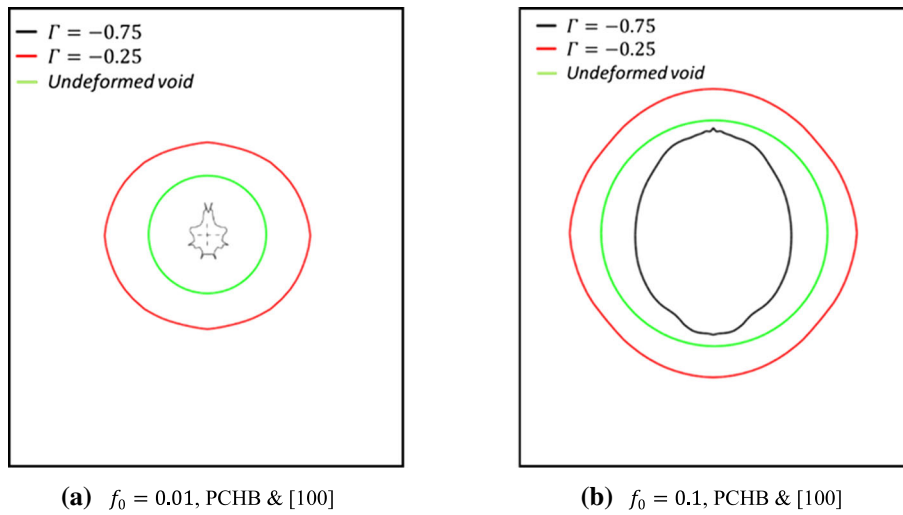
(a) $f_0 = 0.01$, PCHB & [100]   **(b)** $f_0 = 0.1$, PCHB & [100]

Fig. 9 Void growth and shrinkage for two void volume fractions, $f_0 = 0.01$, and $f_0 = 0.1$ at 10% applied strain. The deformation of cross section of void taken on $X_1 - X_2$ mid-plane is shown here
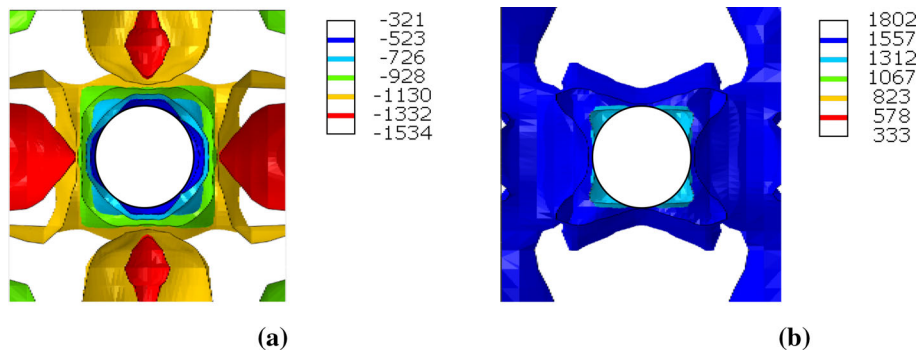

(a)   **(b)**

Fig. 10 Hydrostatic pressure distribution in the vicinity of void for displacement ratio of **a** $\Gamma = -0.25$, $f_0 = 0.01$, and **b** $\Gamma = -0.75$, $f_0 = 0.01$ at 10% applied strain

however non-spheroidal shapes are often idealized as ellipsoid. Hence, spherical and ellipsoidal (prolate and oblate) voids are most widely used in the unit cell studies [6,13,48,51]. However, non-spheroidal shapes are observed in numerical and experimental studies during deformation. The commonly observed non-spheroidal void shapes are diamond [24,52], hexagonal [12], and penny shaped [42]. And super-spheroidal void shapes seen in the earlier studies [45,55] were not highlighted as a separate shape. However, in this study, we see that the factors which result in super-spheroidal void shape are different from the ellipsoidal void shape, and hence it is treated as a separate shape category. The hexagonal void shape seen in the experimental study from Crepin et al. [12], is considered as equivalent to oblate shape as it was seen that the factors resulting in oblate shape were not distinguishable from those resulting in the hexagonal shape. An interesting observation from our results was void spin; void shape evolution with void spin is categorized into an oblate void spin and super-spheroidal void spin.

The spherical void shape is observed for both the displacement ratios of $\Gamma = -0.25 \& -0.75$; all three void volume fractions and ICOs [100] and [110] except for the ICO [111]. The oblate shape was observed only for displacement ratio of $\Gamma = -0.25$, and two void volume fractions of $f_0 = 0.01 \& 0.001$. The void volume fraction $f_0 = 0.1$ and ICO [111] condition did not result in an oblate void shape. The prolate void shape was observed only with higher void volume fraction of $f_0 = 0.1$, and for both displacement ratios. The ICO [111] did not result in a prolate void shape. The diamond shape was observed for the displacement ratio of $\Gamma = -0.25$ and ICO[100]. Super spheroidal shape was primarily observed with a displacement ratio $\Gamma = -0.75$ and for void volume fraction of $f_0 = 0.1 \& 0.01$, whereas the lower void volume fraction of $f_0 = 0.001$ never resulted in the super spheroidal void shape.
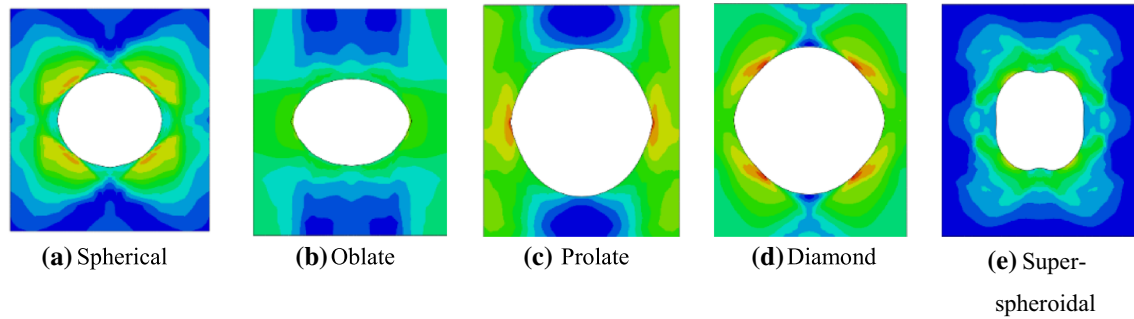
(a) Spherical **(b)** Oblate **(c)** Prolate **(d)** Diamond **(e)** Super-spheroidal

Fig. 11 Void shape categorization

Table 3 List of void shapes resulting from the combination of the parameters

Simulation	Displacement Ratio, Γ	Initial void volume fraction, f_0	Initial Crystallographic Orientation, ICO	Void shape
1	-0.25	0.01	[100]	S
2	-0.25	0.01	[110]	O
3	-0.25	0.1	[100]	D
4	-0.25	0.1	[110]	P
5	-0.75	0.01	[100]	PC
6	-0.75	0.01	[110]	PC
7	-0.75	0.1	[100]	SS
8	-0.75	0.1	[110]	P
9	-0.25	0.01	[111]	O-Sp
10	-0.25	0.1	[111]	SS-Sp
11	-0.25	0.001	[100]	S
12	-0.25	0.001	[110]	O
13	-0.25	0.001	[111]	O-Sp

Where,
S Nearly spherical
O Oblate
P Prolate
D Diamond
SS Super-spheroidal
O-Sp Oblate with void spin
SS-Sp Super-spheroidal with void spin
PC Penny shaped crack

Table 3 summarizes the void shapes obtained for various combinations of parameters. Fig. 12a and b show the void spin observed in our study, two shape evolution which resulted in the void spin were due to ICO [111] and $\Gamma = -0.25$.

Void shrinkage to penny shaped crack was observed for a displacement ratio of $\Gamma = -0.75$. As described in Sect. 4.2, the necessary condition for the void to shrinkage is the presence of positive hydrostatic pressure around the void, and this was observed for all the simulation with the applied displacement ratio of $\Gamma = -0.75$.

4.4 Parameters for tracking void morphology

In this section, an additional parameter is proposed for studying the evolution of void morphology. The existing shape parameter ξ_i, was introduced by Gologanu et al. [12] for studying void shape. The shape parameter ξ_i is found to be useful in describing the spherical and ellipsoidal void shapes but fails to identify other void shapes namely diamond, hexagonal, and super-spheroidal. Hence, we introduce an additional parameter, diagonal distortion. The diagonal distortion, D_{d_i} is defined as

$$D_{d_i} = \ln\left(\frac{R_\phi}{R_i}\right) \tag{15}$$

Where, R_ϕ is the radius at an angle ϕ from the horizontal plane. For the current study, $\phi = 45°$ is considered (see Fig. 13).

(a) Oblate Spin   **(b)** Super-spheroidal spin   **(c)** Penny shape crack
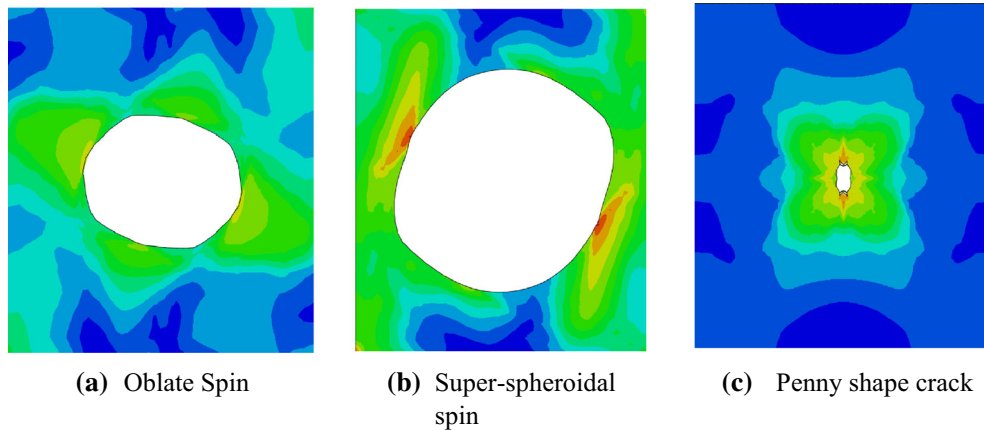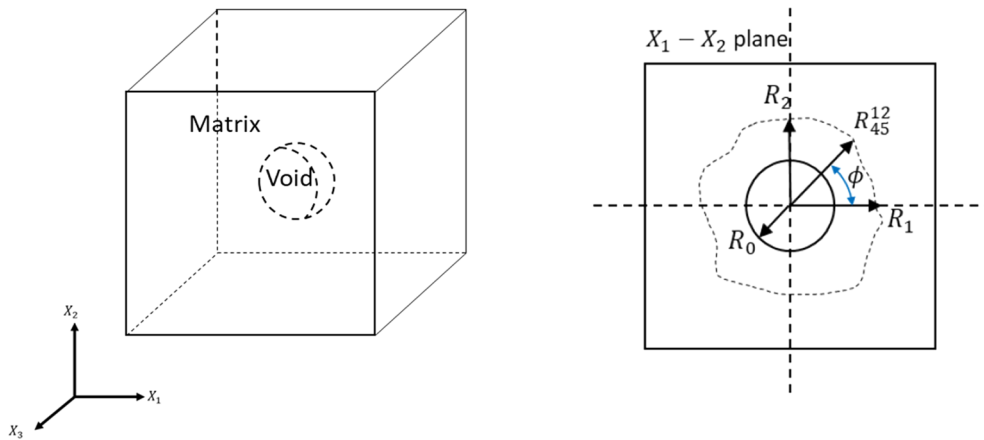
Fig. 12 Void spin and penny shaped crack

Fig. 13 Schematic of the RVE showing the radii used for defining the shape parameter, ξ, and diagonal distortion, D_d

Figure 14a and b presents the evolution of the shape parameter and diagonal distortion for the spheroidal and non-spheroidal void shapes. For spheroidal void shapes such as spherical, prolate, and oblate shapes, two shape parameters ξ_i and D_{d_i} follow a similar trend. E.g., for a prolate void shape evolution, both shape parameters ξ_i and D_{d_i} increases. Table 4 lists the bounds for the shape parameter (ξ_i) and diagonal distortion (D_{d_i}) values for all the void shape evolutions observed in this study. However, for the non-spheroidal void shapes, two parameters are different. Consider a super-spheroidal void shape evolution (see Fig. 14b, the shape parameter initially increases and then falls back to a zero value, indicating that initially void grows into a prolate shape and then at higher plastic deformation void attains a nearly spherical shape. However, the diagonal distortion continuously increases showing a bulging of void at the 45°angle. Similarly, for diamond void shape evolution the shape parameter follows an oblate void shape; however the parameter diagonal distortion shows reduced aspect at 45°angle.

These insights are important for understanding the void coalescences by necking which usually occurs due to shear localization in the ligaments between voids located at 45°. The shape parameter (ξ_i) and along with the proposed parameter diagonal distortion (D_{d_i}) for tracking void shape evolution during ductile failure process contributes towards a better prediction of void coalescence. The detailed study of void coalescence is not in the scope of this study and will be pursued in future.

5 Conclusions

Using crystal plasticity-based finite element analysis, a comprehensive study has been performed to understand the void growth and evolution of void morphology in FCC single crystal. Similar to isotropic material [34]. [40],
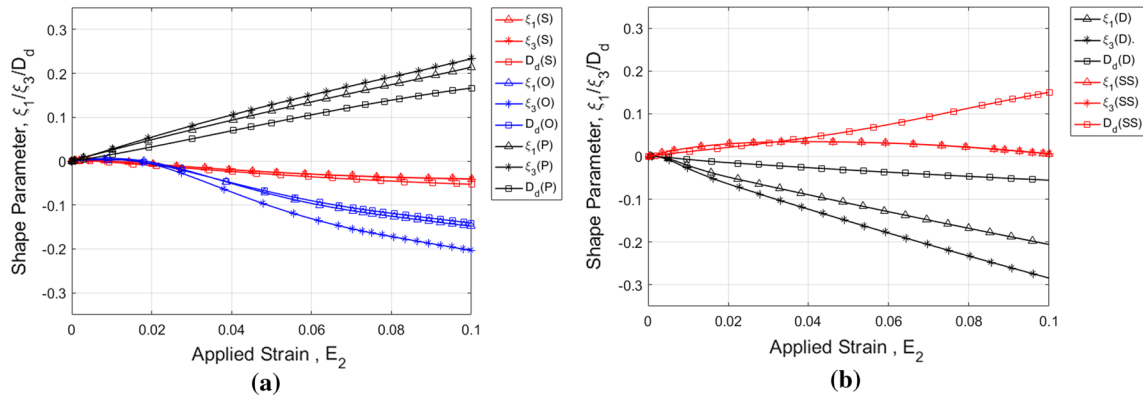
Fig. 14 Shape parameter and diagonal distortion plots for; **a** spheroidal voids and **b** non-spheroidal voids post-deformation

Table 4 Shape parameter and diagonal distortion values for different void shape evolution

Morphology of deformed void	Shape parameter, $\xi_i (i = 1, 3)$	Diagonal distortion, D_{d_1}
Spherical/ Hexagonal	$\xi_1 = \xi_3 = 0.0$	$D_{d_1} \approx 0.0$
Prolate	$\xi_1 \neq \xi_3 > 0.0$	$D_{d_1} > 0.0$
Oblate	$\xi_1 \neq \xi_3 < 0.0$	$D_{d_1} < 0.0$
Diamond/Rhombic	$\xi_1 \neq \xi_3 > 0.0$	$D_{d_1} < 0.0$
Super spheroidal	$\xi_1 \approx \xi_3 \approx 0.0$	$D_{d_1} > 0.0$

even in case of anisotropic material, the void volume fraction is observed to be a significant factor influencing the intensity & spread of the plastic strain near void and the mean void growth. With the decrease in the void volume fraction, the plastic strain intensity & spread increases resulting in the advancement of rapid void growth phase to lower applied strains values. The type of plastic flow observed from our simulations varies from fully plastic flow to plastic flow with elastic region. Fully plastic flow (similar to Gurson's model-1) is observed for smaller to moderate voids, but for larger voids, plastic flow with elastic region (similar to Gurson's model-2) is observed. In general, Gurson's model-1 is found to be a better choice for developing a phenomenological model for anisotropic materials. However, Gurson's model-2 is more appropriate for larger void with boundary conditions leading to cell volume expansion.

In an anisotropic material, ICO with respect to loading direction changes the void growth behavior. ICO introduces an additional elastic and plastic anisotropy over the plastic anisotropy exhibited by the slip system. We choose three ICOs [100], [110], & [111] to study its effect on mean void growth behavior. It is found that the mean void growth obtained for ICO [111] is lower compared to ICOs [100] & [110]. Though this study is representative of void growth in anisotropic material, for a generic ICO [hkl], a more detailed study encompassing entire orientation space is required.

From our study it is observed that void growth results in non-spheroidal void shapes due material anisotropy. However, the existing shape parameter in literature were insufficient to capture non-spheroidal void shapes. To address this scenario, we have introduced an additional shape parameter, "diagonal distortion." Void shape evolution during deformation plays an important role in ductile fracture especially through void coalescence. In here, void growth in anisotropic matrix is discussed in depth and void coalescence will be part of future study.

References

1. Gurson, A.L.: Continuum theory of ductile rupture by void nucleation and growth: Part I- yield criteria and flow rules for porous ductile media. J. Eng. Mater. Technol. **99**(76), 2–15 (1977)
2. Benzerga, A.A., Leblond, J.B., Needleman, A., Tvergaard, V.: Ductile failure modeling. Int. J. Fract. **201**(1), 29–80 (2016)
3. Khan, A., Liu, H.: A new approach for ductile fracture prediction on Al 2024–T351 alloy. Int. J. Plast **35**, 1–12 (2012)

4. Bower, A.F., Wininger, E.: A two-dimensional finite element method for simulating the constitutive response and microstructure of polycrystals during high temperature plastic deformation. J. Mech. Phys. Solids **52**(6), 1289–1317 (2004)
5. Keralavarma, S.M., Benzerga, A.A.: A constitutive model for plastically anisotropic solids with non-spherical voids. J. Mech. Phys. Solids **58**(6), 874–901 (2010)
6. Yerra, S.K., Tekoğlu, C., Scheyvaerts, F., Delannay, L., Van Houtte, P., Pardoen, T.: Void growth and coalescence in single crystals. Int. J. Solids Struct. **47**(7–8), 1016–1029 (2010)
7. Rice, J.R., Tracey, D.M.: On the ductile enlargement of voids in triaxial stress fields. J. Mech. Phys. Solids **17**(3), 201–217 (1969)
8. Nagpal, V., McClintock, F. A., Berg, C. A., Subudhi, M.: Traction-displacement boundary conditions for plastic fracture by hole growth. In *International symposium on foundations of plasticity*, (1972)
9. Needleman, A.: Void growth in an elastic-plastic medium. J. Appl. Mech. **39**(4), 964–970 (1972)
10. Haward, R.N., Owen, D.R.J.: The yielding of a two-dimensional void assembly in an organic glass. J. Mater. Sci. **8**(8), 1136–1144 (1973)
11. Tvergaard, V., Needleman, A.: Analysis of the cup-cone round tensile fracture. Acta Metall. **32**(1), 157–169 (1984)
12. Gologanu, M., Leblond, J.B., Devaux, J.: Approximate models for ductile metals containing non-spherical voids-Case of axisymmetric prolate ellipsoidal cavities. J. Mech. Phys. Solids **41**(11), 1723–1754 (1993)
13. Gologanu, M., Devaux, J., Leblond, J.B.: Approximate models for ductile metals containing nonspherical voids - case of axisymmetric oblate ellipsoidal cavities. J. Eng. Mater. Technol. **116**(July 1994), 290–297 (1994)
14. Monchiet, V., Cazacu, O., Charkaluk, E., Kondo, D.: Macroscopic yield criteria for plastic anisotropic materials containing spheroidal voids. Int. J. Plast **24**(7), 1158–1189 (2008)
15. Monchiet, V., Bonnet, G.: A Gurson-type model accounting for void size effects. Int. J. Solids Struct. **50**(2), 320–327 (2013)
16. Benzerga, A.A., Leblond, J.B.: Effective yield criterion accounting for microvoid coalescence. J. Appl. Mech. Trans. Asme **81**(3), 4–7 (2014)
17. Keralavarma, S.M., Chockalingam, S.: A criterion for void coalescence in anisotropic ductile materials. Int. J. Plast **82**(7), 159–176 (2016)
18. Torki, M.E., Tekoglu, C., Leblond, J.B., Benzerga, A.A.: Theoretical and numerical analysis of void coalescence in porous ductile solids under arbitrary loadings. Int. J. Plast **91**(1), 160–181 (2017)
19. Thomason, P.: Ductile Fracture of Metals. Pergamon Press, Oxford (1990)
20. Tvergaard, V.: Influence of voids on shear band instabilities under plane strain conditions. Int. J. Fract. **17**(4), 389–407 (1981)
21. Xu, W., Ferry, M., Humphreys, F.J.: Spatial morphology of interfacial voids and other features generated at coarse silica particles in nickel during cold rolling and annealing. Scr. Mater. **60**(10), 862–865 (2009)
22. Pushkareva, M., Adrien, J., Maire, E., Segurado, J., Llorca, J., Weck, A.: Three-dimensional investigation of grain orientation effects on void growth in commercially pure titanium. Mater. Sci. Eng., A **671**, 221–232 (2016)
23. Crépin, J., Bretheau, T., Caldemaison, D.: Cavity growth and rupture of β-treated zirconium: A crystallographic model. Acta Mater. **44**(12), 4927–4935 (1996)
24. Madou, K., Leblond, J.B.: A Gurson-type criterion for porous ductile solids containing arbitrary ellipsoidal voids - I: Limit-analysis of some representative cell. J. Mech. Phys. Solids **60**(5), 1020–1036 (2012)
25. Babout, L., Maire, E., Buffière, J., Fougères, R.: Characterization by X-ray computed tomography of decohesion, porosity growth and coalescence in model metal matrix composites. Acta Mater. **49**(11), 2055–2063 (2001)
26. Benzerga, A.A., Besson, J., Pineau, A.: Anisotropic ductile fracture: Part I: experiments. Acta Mater. **52**(15), 4623–4638 (2004)
27. Khan, A.S., Liang, R.: Behaviors of three BCC metals during experiments and modeling. Int. J. Plast **16**, 1443–1458 (2000)
28. Morgeneyer, T.F., Starink, M.J., Sinclair, I.: Evolution of voids during ductile crack propagation in an aluminium alloy sheet toughness test studied by synchrotron radiation computed tomography. Acta Mater. **56**(8), 1671–1679 (2008)
29. Liu, Z.G., Wong, W.H., Guo, T.F.: Void behaviors from low to high triaxialities: transition from void collapse to void coalescence. Int. J. Plast **84**, 183–202 (2016)
30. Gan, Y.X., Kysar, J.W.: Cylindrical void in a rigid-ideally plastic single crystal III: hexagonal close-packed crystal. Int. J. Plast **23**(4), 592–619 (2007)
31. Weck, A., Wilkinson, D.S., Maire, E.: Observation of void nucleation, growth and coalescence in a model metal matrix composite using X-ray tomography. Mater. Sci. Eng., A **488**(1), 435–445 (2008)
32. Lecarme, L., Maire, E., Kumar, A., De Vleeschouwer, C., Jacques, L., Simar, A., Pardoen, T.: Heterogenous void growth revealed by in situ 3-D X-ray microtomography using automatic cavity tracking. Acta Mater. **63**(1), 130–139 (2014)
33. Pushkareva, M., Sket, F., Segurado, J., Llorca, J., Yandouzi, M., Weck, A.: Effect of grain orientation and local strains on void growth and coalescence in titanium. Mater. Sci. Eng., A **760**(January), 258–266 (2019)
34. Koplik, J., Needleman, A.: Void growth and coalescence in porous plastic solids. Int. J. Solids Struct. **24**(8), 835–853 (1988)
35. Xia, L., Fong Shih, C.: Ductile crack growth - I. A numerical study using computational cells with microstructurally-based length scales. J. Mech. Phys. Solids **43**, 233–259 (1995)
36. Xia, L., Fong Shih, C.: Ductile crack growth-II. void nucleation and geometry effects on macroscopic fracture behavior. J. Mech. Phys. Solids **43**(12), 1953–1981 (1995)
37. Xia, L., Fong, S.C., Hutchinson, J.W.: A computational approach to ductile crack growth under large scale yielding conditions. J. Mech. Phys. Solids **43**(3), 389–413 (1995)
38. Ruggieri, C., Panontin, T.L., Dodds, R.H.: Numerical modeling of ductile crack growth in 3-D using computational cell elements. Kluwer Academic Publishers, New York (1996)
39. Kuna, M., Sun, D.Z.: Three-dimensional cell model analyses of void growth in ductile materials. Kluwer Academic Publishers, New York (1996)
40. Faleskog, J., Shih, C.F.: Micromechanics of coalescence - I. Synergistic effects of elasticity, plastic yielding and multi-size-scale voids. J. Mech. Phys. Solids **45**(1), 21–50 (1997)
41. Faleskog, J., Gao, X., Fong Shih, C.: Cell model for nonlinear fracture analysis-I. Micromechanics calibration, (1998)

42. Schacht, T., Untermann, N., Steck, E.: The influence of crystallographic orientation on the deformation behaviour of single crystals containing microvoids. Int. J. Plast **19**, 1605–1626 (2003)
43. Potirniche, G.P., Hearndon, J.L., Horstemeyer, M.F., Ling, X.W.: Lattice orientation effects on void growth and coalescence in fcc single crystals. Int. J. Plast **22**(5), 921–942 (2006)
44. Yang, M., Dong, X.: Simulation of lattice orientation effects on void growth and coalescence by crystal plasticity. Acta Metall. Sin. Engl. Lett. **22**(1), 40–50 (2009)
45. Ha, S., Kim, K.: Void growth and coalescence in f.c.c. single crystals. Int. J. Mech. Sci. **52**(7), 863–873 (2010)
46. Ling, C., Besson, J., Forest, S., Tanguy, B., Latourte, F., Bosso, E.: An elastoviscoplastic model for porous single crystals at finite strains and its assessment based on unit cell simulations. Int. J. Plast **84**(1), 58–87 (2016)
47. Garrison, W., Wojcieszynski, A., Iorio, L.: Recent advances in fracture, In *The Minerals, Metals, and Materials Society*, Florida, (1997)
48. Garrison Jr., W.M., Moody, N.: Ductile fracture. J. Phys. Chem. solids **48**, 1035–1074 (1987)
49. Chezan, A.R., De Hosson, J.: Superplastic behavior of coarse-grained aluminum alloys. Mater. Sci. Eng. A **410–411**, 120–123 (2005)
50. Pardoen, T., Hutchinson, J.W.: An extended model for void growth and coalescence. J. Mech. Phys. Solids **48**, 2467–2512 (2000)
51. Ragab, A.R.: Application of an extended void growth model with strain hardening and void shape evolution to ductile fracture under axisymmetric tension. Eng. Fract. Mech. **71**(11), 1515–1534 (2004)
52. Ragab, A.R.: A model for ductile fracture based on internal necking of spheroidal voids. Acta Mater. **52**(13), 3997–4009 (2004)
53. Huang, Y.: Accurate dilatation rates for spherical voids in triaxial stress fields. Trans. ASME **58**, 1084–85 (1991)
54. Besson, J.: Continuum models of ductile fracture: a review **19**, 3–52 (2010)
55. Tvergaard, V., Nyvang Legarth, B.: Effects of anisotropy and void shape on cavitation instabilities. Int. J. Mech. Sci. **152**, 81–87 (2019)
56. Hill, R.: Generalized constitutive relations for incremental deformation of metal crystals by multislip. J. Mech. Phys. Solids **14**(2), 95–102 (1966)
57. Hill, R., Rice, J.R.: Constitutive analysis of elastic-plastic crystals at arbitrary strain. J. Mech. Phys. Solids **20**(6), 401–413 (1972)
58. Asaro, R.J.: Crystal Plasticity. J. Appl. Mech. **50**(4b), 921 (1983)
59. Huang, Y.: A user-material subroutine incorporating single crystal plasticity in the ABAQUS finite element program, Mech Report 178, Harvard University (1991)
60. Kysar, J. W., Hall, P.: Addendum to A User-Material Subroutine Incorporating Single Crystal Plasticity in the ABAQUS Finite Element, Mech Report 178, Harvard University (1997)
61. Peirce, D., Asaro, R.J., Needleman, A.: An analysis of nonuniform and localized deformation in ductile single crystals. Acta Metall. **30**(6), 1087–1119 (1982)
62. Chang, Y.W., Asaro, R.J.: Lattice rotations and localized shearing in single crystals. Arch. Mech. **32**(3), 369–388 (1980)
63. Bower, A.F.: Applied Mechanics of Solids. CRC Press, Boca Raton (2009)
64. Shu, J.Y.: Scale-dependent deformation of porous single crystals. Int. J. Plast **14**(10–11), 1085–1107 (1998)
65. Jacobsen, E.H.: Elastic spectrum of copper from temperature-diffuse scattering of X-Rays. Phys. Rev. **97**(3), 654–659 (1954)
66. Bridgman, P. W.: Studies in large plastic flow and fracture: with special emphasis on the effects of hydrostatic pressure, New York, p. 362 (1952)
67. McMeeking, R.M.: Finite deformation analysis of crack-tip opening in elastic-plastic materials and implications for fracture. J. Mech. Phys. Solids **25**(5), 357–381 (1977)
68. Budiansky, B., Hutchinson, J.W., Slutsky, S.: Void growth and collapse in viscous solids, Division of applied sciences. Harvard university, Cambridge (1982)